

Article

Additive Manufacturing Potentials of High Performance Ferritic (HiperFer) Steels

Torsten Fischer ^{1,*} , Bernd Kuhn ¹ , Xiuru Fan ^{1,2} and Markus Benjamin Wilms ^{3,4} 

¹ Institute of Energy and Climate Research (IEK), Microstructure and Properties of Materials (IEK-2), Forschungszentrum Jülich GmbH, 52425 Jülich, Germany; b.kuhn@fz-juelich.de (B.K.); x.fan@fz-juelich.de (X.F.)

² Central Iron & Steel Research Institute (CISRI) Group, Material Digital R&D Centre, Beijing 100081, China
³ Materials Science and Additive Manufacturing, School of Mechanical Engineering and Safety Engineering, University of Wuppertal, 42119 Wuppertal, Germany; mwilms@uni-wuppertal.de

⁴ Fraunhofer-Institute for Laser Technology (ILT), 52074 Aachen, Germany

* Correspondence: t.fischer@fz-juelich.de; Tel.: +49-2461-61-5096

Featured Application: Empowering metal additive manufacturing by unveiling the economic potentials of novel, low-cost alloys with improved mechanical properties (e.g., in comparison to conventional AM alloys, such as AISI 316L) and capable of in-built heat-treatment. Improvement of the quality of AM-processed material via the implementation of microstructural mechanisms for actively counterbalancing AM-process-related manufacturing flaws (pores, cavities).

Abstract: In the present study, the first tailored steel based on HiperFer (high-performance ferrite) was developed specifically for the additive manufacturing process. This steel demonstrates its full performance potential when produced via additive manufacturing, e.g., through a high cooling rate, an in-built heat treatment, a tailored microstructure and counteracts potential process-induced defects (e.g. pores and cavities) via “active” crack-inhibiting mechanisms, such as thermomechanically induced precipitation of intermetallic $(\text{Fe,Cr,Si})_2(\text{W,Nb})$ Laves phase particles. Two governing mechanisms can be used to accomplish this: (I) “in-built heat treatment” by utilizing the “temper bead effect” during additive manufacturing and (II) “dynamic strengthening” under cyclic, plastic deformation at high temperature. To achieve this, the first HiperFer^{AM} (additive manufacturing) model alloy with high precipitation kinetics was developed. Initial mechanical tests indicated great potential in terms of the tensile strength, elongation at rupture and minimum creep rate. During the thermomechanical loading, global sub-grain formation occurred in the HiperFer^{AM}, which refined the grain structure and allowed for higher plastic deformation, and consequently, increased the elongation at rupture. The additive manufacturing process also enabled the reduction of grain size to a region, which has not been accessible by conventional processing routes (casting, rolling, heat treatment) so far.

Keywords: additive manufacturing (AM); laser metal deposition (LMD); HiperFer^{AM}; temperbead-effect; in-built heat treatment



Citation: Fischer, T.; Kuhn, B.; Fan, X.; Wilms, M.B. Additive Manufacturing Potentials of High Performance Ferritic (HiperFer) Steels. *Appl. Sci.* **2022**, *12*, 7234. <https://doi.org/10.3390/app12147234>

Academic Editor: Sasan Dadbakhsh

Received: 29 June 2022

Accepted: 15 July 2022

Published: 18 July 2022

Publisher's Note: MDPI stays neutral with regard to jurisdictional claims in published maps and institutional affiliations.



Copyright: © 2022 by the authors. Licensee MDPI, Basel, Switzerland. This article is an open access article distributed under the terms and conditions of the Creative Commons Attribution (CC BY) license (<https://creativecommons.org/licenses/by/4.0/>).

1. Introduction

Up to now, mainly established commercial materials have been applied in additive manufacturing. Materials that have been tailored for AM processes (including mutual process optimization) are still underrepresented in international R&D efforts. The main reasons for this are high development expenses and a still relatively limited market. In order to improve the applicability of AM, the economic efficiency of both the materials and processes have to be increased. In this paper, a material is presented that benefits from the additive manufacturing process and can be customized to desired applications not only by varying chemical composition but also by variations in AM process parameters. Process parameters,

such as beam diameter, laser power and scan speed, determine the shape and size of the melt pool formed by alternating the laser absorption ratios [1,2]. Solidification conditions of the melt pool are controlled by the heat dissipation mechanisms [3], which are influenced by material properties, geometrical aspects and temperature distribution in the printed material [4]. The characteristic high solidification rates encountered in additive manufacturing processes typically result in the formation of supersaturated solid solutions, making a post-process heat treatment necessary [5]. However, in additive manufacturing, adjustments of the process parameters may induce in-process precipitation reactions [6–9], phase transformations [10,11], affect residual stress in the printed parts [12–15], and modify the grain structure and texture [5,16,17]. Thus, mechanical properties, e.g., tensile and fatigue strength, can be significantly altered by the utilization of different process parameters [14,18–21]. Process parameters also have a decisive impact on defect formation, the final density, and thus, the material integrity. Residual porosity is a key factor for the mechanical and technological properties of additively manufactured materials because process-related pores [21–24] can act as crack initiators [9]. So far, the approach to overcoming the residual porosity is the optimization of process control. Advanced detectors and monitoring software are being developed to control production quality [9]. Often post-treatment procedures, such as hot isostatic pressing, are necessary to reduce porosity, which constitute an economical drawback.

Partially counteracting process-related material defects by utilizing material's inherent microstructural crack-obstruction mechanisms, so that component defects can be tolerated to a certain extent, would be a highly innovative approach. The novel, high-chromium ferritic HiperFer (high-performance ferrite) steels developed at Forschungszentrum Jülich GmbH [25,26] are suitable material candidates to achieve this for several reasons: strengthening via a combination of solid solution and precipitation hardening by intermetallic Laves phase particles ((Fe,Cr,Si)₂(Nb,W)) [25]. "Dynamic strengthening" of HiperFer is accomplished via thermomechanically induced precipitation [27] of the Laves phase using conventional processing [28–31] under in-service conditions [32,33]. How effectively crack initiation is inhibited/delayed in Laves phase strengthened ferritic steel was demonstrated using thermomechanical fatigue (TMF) experiments on Crofer[®]22 H, the predecessor alloy of HiperFer (cf. [33] for details). The fatigue curve of Laves-phase-strengthened steel typically consists of three phases [33]: an initial phase of pronounced strengthening (which makes up for about 1% of the fatigue life), a stable phase (which lasts until approximately half of the fatigue life) and a comparatively protracted damage phase (making up for approximately the other half of fatigue life). During the damage phase, a comparatively small decrease in stress range per cycle is observed because cyclic plasticization dislocations are generated, leading to both non-permanent strain hardening and accelerated nucleation of intergranular Laves phase particles. As a result of the effective blocking of the dislocations by the deformation-induced Laves phase particle precipitation (under the experimental conditions lined out in [33], the total number of Laves phase particles in Crofer[®]22 H, for example, increased from 0 to 4576 during testing from 10 to 2000 TMF cycles), part of the dislocation-induced strain hardening remains practically permanent. For a detailed explanation of the mechanisms and the complete evolution of intragranular Laves phase precipitates in Laves-phase-strengthened ferritic steel during TMF loading, [33,34] may be consulted.

Furthermore, high chromium ferritic steels generally possess good resistance to (high-temperature) corrosion due to the formation of a protective duplex Cr₂O₃/(Mn, Cr)₃O₄ scale on the component surface [35]. The chromium content of HiperFer was adjusted to 17 wt.% to exclude the undesired formation of the FeCr σ -phase at temperatures above 600 °C [25], and thus, the potential danger of embrittlement due to long-term service at elevated temperatures.

With this property profile, an alloy that is custom designed for additive manufacturing on the basis of HiperFer is a good candidate to replace typical austenitic grades, such as AISI 316L, at much lower material and processing costs. A suitable way to make the dynamic strengthening properties of HiperFer steel accessible for in-build and in-service

strengthening of AM-processed components is tuned precipitation kinetics. Based on the outlined mechanisms, a first HiperFer^{AM} (additive manufacturing) alloy was created specifically for additive manufacturing processes, which ideally should utilize both the “dynamic strengthening” and the so-called “temper bead-effect” [36–39] for in-build heat treatment (to make downstream heat treatments obsolete). In this instance, a suitable in-build heat treatment was aimed at keeping the residual stresses below the yield strength of the material and simultaneously generating Laves-phase-strengthened precipitates. In addition, the paper outlines the obtained mechanical property data, such as tensile strength, elongation at rupture and minimum creep rates (depending on the build direction). Furthermore, the active deformation mechanisms in additively processed material were compared to conventionally manufactured (casting, rolling, heat treatment) material.

2. Materials and Methods

2.1. Laves-Phase-Strengthened Ferritic HiperFer Steel

The HiperFer trial steel 17Cr2 was vacuum induction melted (by the Steel Institute of RWTH Aachen University, Germany). The resulting ingot was hot-rolled to 15 mm thick plate material in the temperature range from 1000 to 920 °C and subsequently precipitation annealed (0.5–10 h/600–650 °C). The chemical compositions of HiperFer 17Cr2 and laser metal deposition (LMD)-manufactured HiperFer^{AM} are given in Table 1.

Table 1. Chemical compositions of Laves-phase-strengthened ferritic trial steels (wt.-%).

	C	S	N	Cr	Ni	Mn	Si	Mo	Ti
22 A	0.004	<0.001	0.002	22.8	-	0.44	0.02	-	0.06
	Nb	W	Cu	Fe	P	Al	Mg	Co	La
	<0.01	-	-	Balance	-	0.013	-	-	-
HiperFer 17Cr2 *	C	S	N	Cr	Ni	Mn	Si	Mo	Ti
	<0.003	<0.001	<0.003	17–18	-	0.2–0.5	0.2–0.3	-	-
	Nb	W	Cu	Fe	P	Al	Mg	Co	La
	0.5–0.6	2.4–2.6	-	Balance	-	-	-	-	-
HiperFer ^{AM}	C	S	N	Cr	Ni	Mn	Si	Mo	Ti
	0.0033	<0.0008	0.0017	19.152	-	0.365	1	-	0.05
	Nb	W	Cu	Fe	P	Al	Mg	Co	La
	1.5	2	-	Balance	-	-	-	-	-

* [40].

2.2. LMD-Manufactured HiperFer^{AM}

The base HiperFer^{AM} powder material was manufactured from gas-atomized experimental 22 A powder (chemical composition listed in Table 1). Since 22 A powder was utilized as the base composition, the first HiperFer^{AM} alloy featured a higher chromium content than HiperFer 17Cr2 (cf. Table 1).

The final powder material was manufactured by blending the 22 A powder with high-purity Si, Nb and W powders in a Turbula σ -mixing device (WAB GmbH) for 30 min. As a substrate material, a tool steel (AISI H10, 1.2365) was used, which was sand-blasted and cleaned with ethanol prior to deposition. LMD processing was conducted with two individual 5-axis handling systems, both using fiber-coupled diode lasers (Laserline GmbH, Mülheim-Kärlich, Germany). For the large beam diameter (3 mm), also referred to as the low “power density” in Table 2, an LDM3000-60 laser, emitting laser radiation with a wavelength of 976 nm (beam parameter product (BPP): 60 mm \cdot mrad), was used. The laser beam was coupled into an optical fiber with a core diameter of 600 μ m (NA = 0.2) and subsequently shaped using collimation ($f_{c, 3 \text{ mm}} = 65 \text{ mm}$) and focusing lenses ($f_{f, 3 \text{ mm}} = 230 \text{ mm}$). The smaller beam diameter (0.66 mm) was created by using an LDF2000-30 diode laser system, simultaneously emitting laser radiation with 1025 nm and 1064 nm. Beam shaping after the optical fiber (core diameter: 600 μ m, NA = 0.2) was enabled using a combination of collimation ($f_{c, 0.66 \text{ mm}} = 200 \text{ mm}$) and focusing lenses ($f_{f, 0.66 \text{ mm}} = 182 \text{ mm}$). The powder

material was fed pneumatically with argon gas via a disc-based feeding system (Sulzer-Metco Twin 10C, OC Oerlikon AG, Pfäffikon, Switzerland) through a coaxial 3-jet nozzle (D40-type, Fraunhofer ILT, Aachen, Germany). For melt pool shielding, argon gas was used, which was fed through the tip of the coaxial powder nozzle. The HiperFer^{AM} powder blend was processed with the process parameters shown in Table 2.

Table 2. HiperFer^{AM} LMD process parameters.

Process Parameter	Low Power Density (“LPD”)	High Power Density (“HPD”)
Area-specific laser power	195 Wmm ⁻²	1050 Wmm ⁻²
Feed speed	400 mm/min	1500 mm/min
Laser power	1375 W	360 W
Powder mass flow rate	11.3 g/min	2.4 g/min
Track offset	2.3 mm	0.35 mm
Height offset	1.4 mm	0.3 mm
Beam diameter	3 mm	0.66 mm
Deposition strategy	Unidirectional	Unidirectional
Nozzle type	3-jet nozzle	3-jet nozzle
Shielding gas	Argon	Argon

2.3. Mechanical Testing

Tensile experiments at ambient temperature were conducted on miniature size specimens (thread size: M5, $l = 42$ mm, $l_0 = 20$ mm and $d_0 = 3$ mm) according to DIN EN ISO 6892-1 (constant strain rate $\dot{\epsilon} = 10^{-3} \text{ S}^{-1}$) [41] utilizing an Instron 1381 type testing machine with 10 kN of load capability. At 650 °C, tensile tests were carried out according to DIN EN ISO 6892-2 [42]. In accordance with the standard, a strain rate of $\dot{\epsilon}_{el} = 8.33 \times 10^{-5} \text{ S}^{-1}$ was applied in the elastic deformation range, while in the plastic range, a strain rate of $\dot{\epsilon}_{pl} = 8.33 \times 10^{-4} \text{ S}^{-1}$ was utilized. All tensile specimens were electrically discharge machined (EDM) from the HiperFer^{AM} LMD samples in the building (Z) direction (Figure 1).

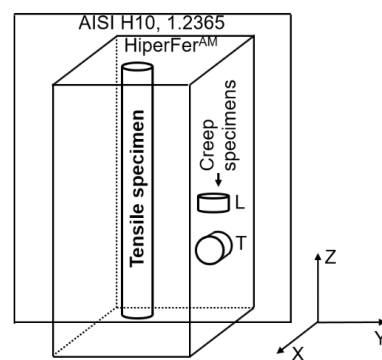


Figure 1. Schematic representation of electrical discharge machining of mechanical testing specimens from HiperFer^{AM} LMD samples: creep specimens were taken from both the longitudinal and transversal directions, while tensile specimens were taken from the longitudinal direction only.

Stepped increasing stress (70, 100, 120, 130 MPa) compression creep experiments were performed on miniature cylindrical specimens ($d: 3$ mm, $h: 3.5$ mm) at 650 °C by applying an Instron 1381 testing machine (Instron, Darmstadt, Germany) that was equipped with all-ceramic loading and strain measurement set-ups. The testing stress was incrementally increased upon entry of a quasi-secondary creep stage or after 150 h of holding at each stress level. Temperatures were controlled to an accuracy of ± 1 °C using type S thermocouples attached to the specimens' gauge length in the creep experiments. The strain measurement was performed with a digital 5 mm strain transducer (Solartron, accuracy: 1.1 μm (peak to peak error)). The compression creep specimens were EDM from the longitudinal (L)

and transversal (T) directions in relation to the build direction from the HiperFer^{AM} LMD samples (Figure 1).

Vickers hardness tests (HV1) were performed according to DIN EN ISO 6507 [43] by applying a Qness A10+ hardness tester (ATM Qness GmbH, Mammelzen, Germany).

2.4. Microstructural Investigation

Samples for microstructural analysis were cut from the HiperFer^{AM}, hot embedded, ground and polished to a sub-micron finish in a colloidal silica suspension and Al₂O₃ in dilute KOH solution for approx. 4 h. Electrolytic etching at 1.5 V in 5% H₂SO₄ was subsequently performed to enhance the particle/matrix contrast. A Zeiss Merlin field emission scanning electron microscope (FESEM) was utilized for high-resolution microstructural investigations.

The small size of the early stage Laves phase precipitates and the magnetic properties of HiperFer steels make detailed analysis using traditional methods inaccurate and time-consuming. For this reason, particle analysis was performed using quantitative image analysis. Particle analysis was conducted at 2 representative sample positions. Grain boundaries and particle-free zones were excluded in the determination of particle density. The size distributions of Laves phase particles were determined using “background corrected” SEM images (accomplished applying the “Count and measure for Olympus Stream” package in the Olympus Stream Desktop 2.4 commercial software). Subsequently, the mean value of the data was used as the analysis result. A detailed description of the particle analysis is given in [44].

Additionally, samples for EBSD analysis were prepared from the mechanical testing specimens. EBSD analysis was performed using a Zeiss Merlin SEM equipped with an Oxford Instruments EBSD system (NORD LYS 2 camera) and energy dispersive X-ray spectroscopy (EDS, EDX, X Max 150).

3. Results and Discussion

HiperFer steel owes its strength to a combination of solid solution strengthening and precipitation hardening using thermodynamically stable (Fe, Cr, Si)₂(Nb, W) Laves phase particles [25]. Nb and Si are key elements in Laves phase precipitation: Nb is used because when combined in an alloy with tungsten, it improves solid solution strengthening to some extent [45]. Furthermore, it is a strong Laves phase former [46], and because of its comparatively low solubility and high diffusion rate, it facilitates precipitation in ferrite. Si further accelerates nucleation [46–50] of the Laves phase [25,35,46,51] precipitates. Figure 2 depicts the solid solution strengthening effects of W and Nb in HiperFer steel. The figure indicates a more pronounced impact of W on UTS and a greater impact of Nb on YS_{0.2}.

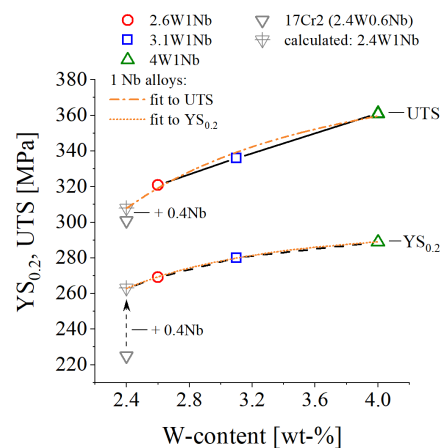


Figure 2. Impact of W and Nb in solid solution on ambient temperature tensile strength values with a virtual 2.4W1Nb alloy, equation: $YS_{0.2} = a \times (1 - cW - b)$; cW : W-content in wt.%, a : 300.05, b : 2.38; $UTS = a \times (1 - cW - b)$; cW : W-content in wt.%, a : 396.53, b : 1.71 [31].

In the case of a 17Cr2 base alloy (2.4W0.6Nb), $YS_{0.2}/UTS$ values of 400/660 MPa were achieved in the precipitation heat-treated state [33].

Increasing the W and Nb contents improved the solid solution strengthening effect, along with increasing the volume fraction and reducing the average particle size of the Laves phase precipitates, resulting in enhanced mechanical properties, in particular creep strength [31]. Figure 3 displays the effects of varying the W and Nb contents on the calculated limit stress for dislocation creep σ_{th} (for details cf. [31,52]): using W and Nb alloying, an increase in the limit stress of approximately 61% was achievable.

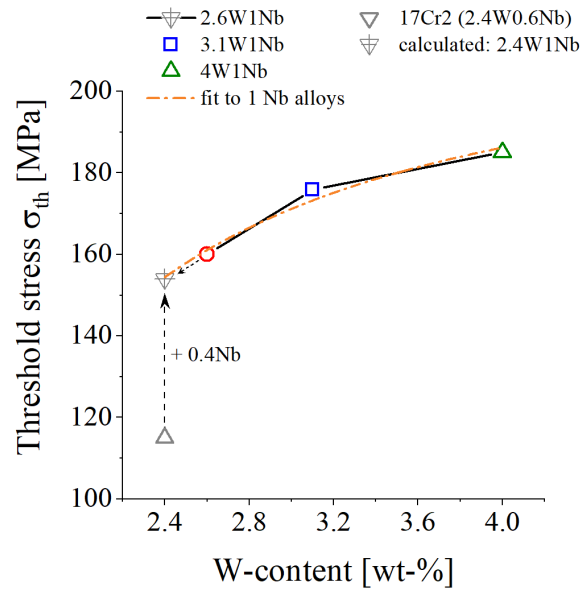


Figure 3. Impact of W and Nb on the threshold stress σ_{th} [31].

The addition of Si mainly resulted in a reduction in the Laves particle size, increased the number of particles and accelerated the precipitation kinetics [53]. From the evaluated increase in limit stress for dislocation creep σ_{th} by Si-alloying (Figure 4), it could be derived that by Si alloying, an approximate increase of 43% was obtainable.

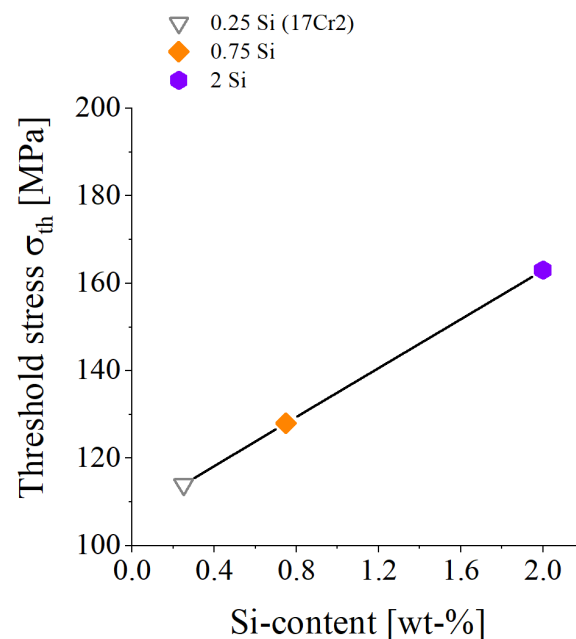


Figure 4. Effect of Si on σ_{th} [54].

Based on these results, the Nb/Si contents were adjusted to 1.5/1 wt.% in order to maximize the (i) precipitation kinetics and (ii) volume fraction and to decrease the particle size in the HiperFer^{AM} (Table 1) trial alloy. Because of the high melting point discrepancy between W and the other constituents, a moderate content of W (2 wt.%) was chosen to alleviate the expected difficulties in the additive manufacturing process.

The increased Nb and Si contents (compared with conventionally casted, rolled and heat-treated HiperFer 17Cr2 (Table 1)), in combination with the high cooling rates of the AM process, resulted in a highly supersaturated solid solution alloy matrix in the as-built state, which in turn led to rapid precipitation kinetics as a result of the high precipitation pressure toward equilibrium. Despite comparatively short high-temperature periods, the in-build (i.e., temper bead) heat treatment (Figure 5) successfully produced a large amount of finely dispersed intragranular Laves phase particles. In addition, the high angle grain boundaries (HAGb) were covered by Laves phase precipitates, which stabilized the grain structure without embrittling the material. The stabilization of the grain structure is the key factor that allows for dynamic strengthening [27,55] under fatigue loading. Dynamic hardening/precipitation was successfully exploited in aluminum alloys AA2021, AA6061 and AA7050 to enhance high-cycle fatigue performance [56]. For this purpose, additional fine particles were generated in the particle free zones (PFZs) using suitable cyclic training. In the fully precipitated state (highest strength state), no dynamic precipitation was observed under cyclic loading in these aluminum alloys. This, however, was achieved in the HiperFer and HiperFer^{AM} type alloys.

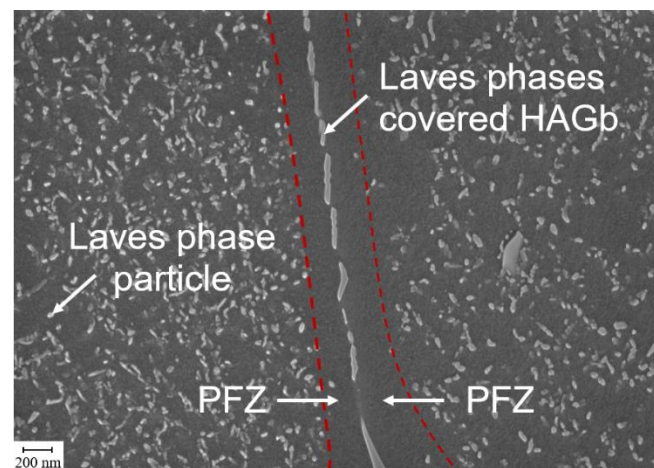


Figure 5. Microstructural features of LMD-manufactured HiperFer^{AM} (LPD variant, further process parameters, cf. Table 2).

Process-induced pores that are contained in additively manufactured materials can act like notches and cause an accumulation of plastic strain in the surrounding material under cyclic loading. In steels of the HiperFer type, this induces thermomechanically induced precipitation [28,32] of Laves phase particles at these dislocations at high temperature, which strengthen the vicinity of pores and actively obstruct crack propagation.

Within the scope of this study, it was investigated to which degree microstructure characteristics (grain size, particle number, size, etc.) can be influenced “in-build” by varying the AM process parameters. For this purpose, the area-specific laser powers of 195 and 1050 W/mm² were chosen. HiperFer^{AM} manufactured with a specific laser power input of 195 W/mm² in the following is referred to as the low-power-density (LPD) variant, while an energy input of 1050 W/mm² was the high-power-density (HPD) variant. Further AM parameter variations are summarized in Table 2.

The typical microstructure of recrystallized and quality heat-treated ferritic, Laves-phase-strengthened steels consists of globular grains with particle-free zones (varying from 200–2000 nm in width, depending on the chemistry and temperature/stress history) along

HAGBs (Figure 6). Near the PFZ (“IG_{Exterior}” region in Figure 6), the particles were usually slightly smaller. Gradual particle dissolution was argued to be the reason for this particular feature. The elements dissolving into the matrix diffuse toward the grain boundary and gradually coarsen the Laves phase particles located there. Accordingly, the particles in the grain interior (“IG_{center}” region in Figure 6) were found to be larger [11].

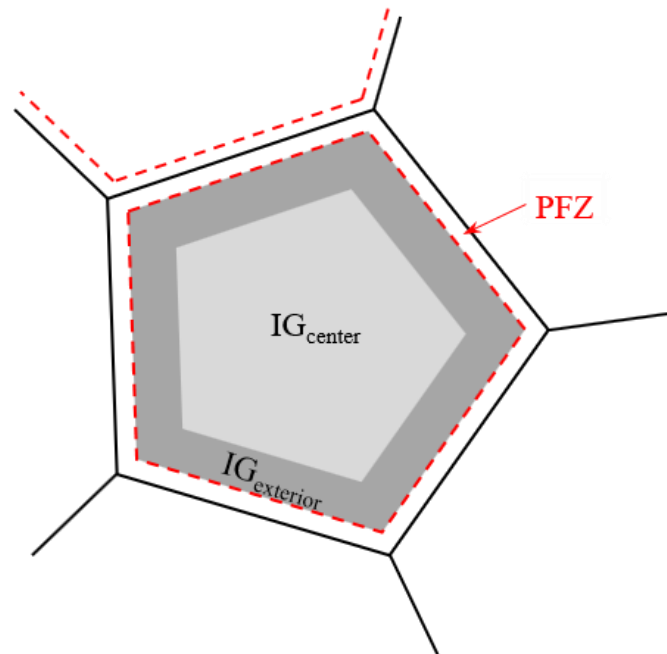


Figure 6. Schematic representation of the typical microstructure of recrystallized and quality heat-treated ferritic Laves-phase-strengthened steel [30].

Large, aligned, rod-shaped grains were predominantly observed in the LPD-manufactured HiperFer^{AM}, while only a small area of aligned, even smaller rod-shaped grains was encountered in the HPD variant (Figure 7) where the globular grain shape prevailed (Figure 7b). This demonstrated that the grain size could readily be adjusted by varying the AM processing parameters. Conventionally processed HiperFer 17Cr2 typically prevails in a grain size of approx. 500 μm , while both applied AM parameter sets resulted in predominantly globular grains in the size region of approx. 200 μm and less (Figure 8). However, incompletely melted tungsten clusters were observed (cf. Figure 7). An additional processing-related issue was SiO₂ particles. These particles tended to be larger and more numerous in the LPD variant than in the HPD variant (cf. Figure 7). Finley-distributed SiO₂ particles were also observed in LPBF-manufactured 316L [9].

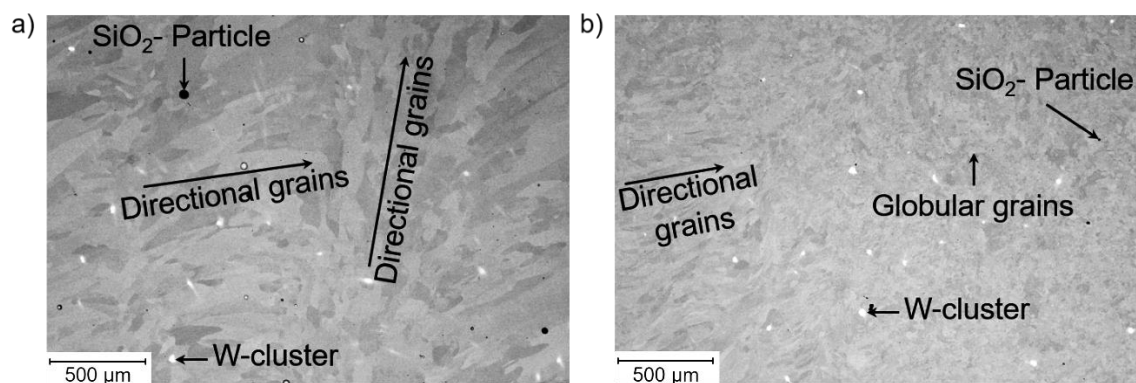


Figure 7. SEM micrographs of LMD-manufactured HiperFer^{AM} in the as-built state: (a) LPD and (b) HPD variants.

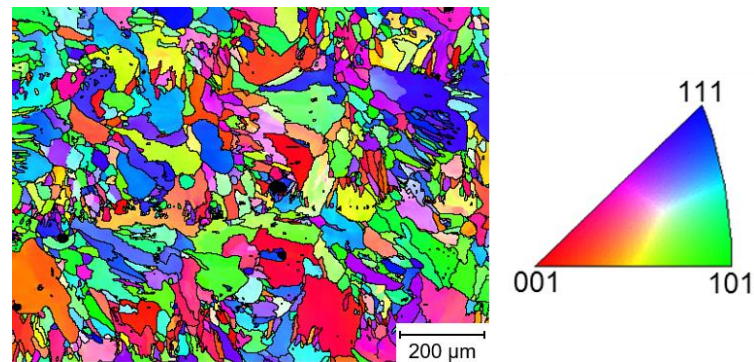


Figure 8. EBSD-IPF (inverse pole figure) micrograph of the LMD-manufactured HiperFer^{AM} HPD variant in the as-built state (reproduced from [9]).

In the future, this can be prevented via the preparation of a master alloy from which the AM powder will be produced. Moreover, the change in power density resulted in a different number and size of Laves phase particles (cf. Figure 9). In the LPD material, the area-specific total number of particles in the as-built state was more than twice that of the HPD variant (cf. Figures 9 and 10a). The particle size classification demonstrated a clear tendency toward larger particle diameters in the HPD variant. The proportion of particles below 20 nm was lower by more than a factor of 5 in the HPD variant (Figure 10b). The lower power input explained the tendency toward the smaller particle size in the case of the LPD variant well. In addition to the higher power input, a smaller beam diameter was applied in the case of the HPD manufactured material. For this reason, more surface area was re-melted and material cooling was slower, i.e., more heat and time were available for particle growth.

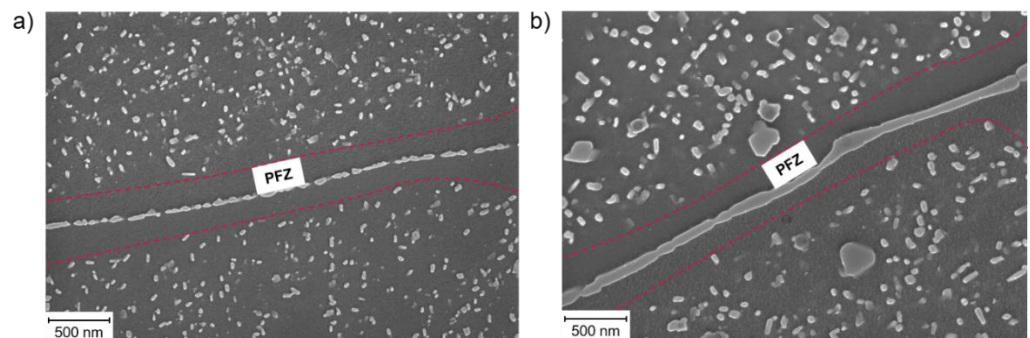


Figure 9. Laves phase particles in LMD-manufactured HiperFer^{AM}: (a) LPD and (b) HPD variants.

In conventionally fabricated HiperFer 17Cr2 (recrystallized and precipitation annealed for 2 h at 650 °C), the highest area-specific particle number was observed (Figure 10a). Considering the time necessary for Laves phase precipitation, the advantage of HiperFer^{AM} clearly emerged: While the heat treatment of HiperFer 17Cr2—including recrystallization and precipitation annealing—took more than 2 h, the heat treatment of HiperFer^{AM} was carried out in situ despite re-melting in the range of seconds. In HiperFer 17Cr2, as in the LPD manufactured HiperFer^{AM}, particle fractions smaller than 20 nm and between 20 and 40 nm were formed (Figure 10b).

The width of the PFZs (approximately 300 nm) in HiperFer^{AM} was found to be independent of the area-specific laser power. Larger parameter field studies are required to evaluate to what extent the PFZ width can be tuned by the in-build heat treatment, which may have a direct effect on material ductility.

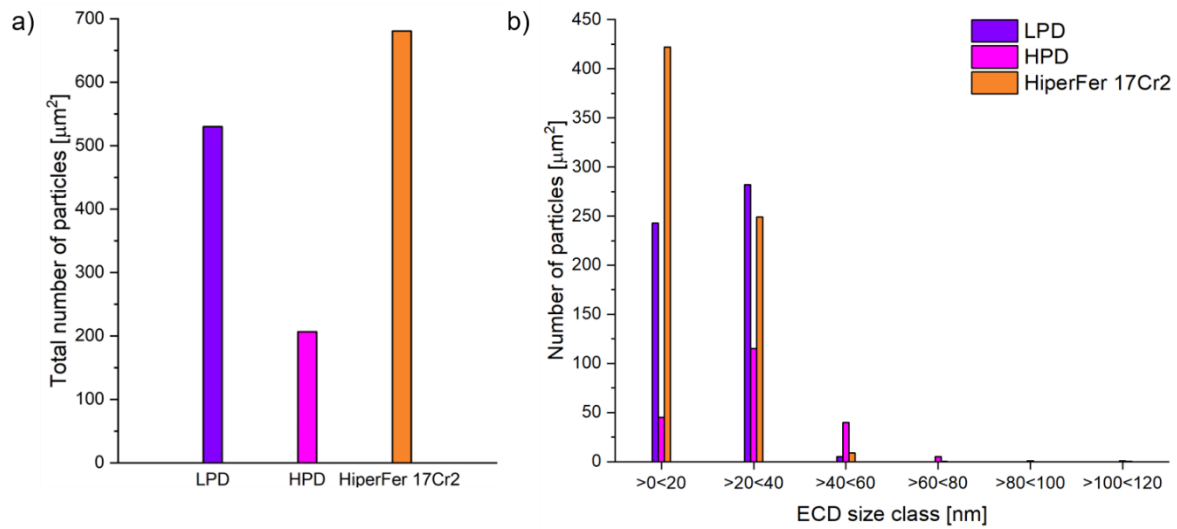


Figure 10. (a) Area-specific total number of particles in the as-built LPD and HPD HiperFer^{AM} and conventional HiperFer 17Cr2 Pa (2 h 650 °C) materials and (b) corresponding size classification by equivalent circle diameter (ECD).

Regions of varying particle size, such as the “IG_{Exterior}” and “IG_{center}” regions typically encountered in conventionally fabricated HiperFer (Figure 6), were not observed in HiperFer^{AM}. This was caused by the shorter cumulated time at high temperatures and the absence of soaking.

Tensile tests were carried out to characterize the macroscopic impact of the microstructures generated in-build. The resulting UTS and total strain at rupture are depicted in Figure 11, while the corresponding values are listed in Table 3. In comparison to conventionally (rolled, recrystallized, precipitation annealed (650 °C/2 h)) produced 17Cr2 sheet material, the ambient temperature tensile strength values of LMD-processed HiperFer^{AM} were found to be higher (UTS_{HPD}: + 107 MPa, UTS_{LPD}: + 14 MPa).

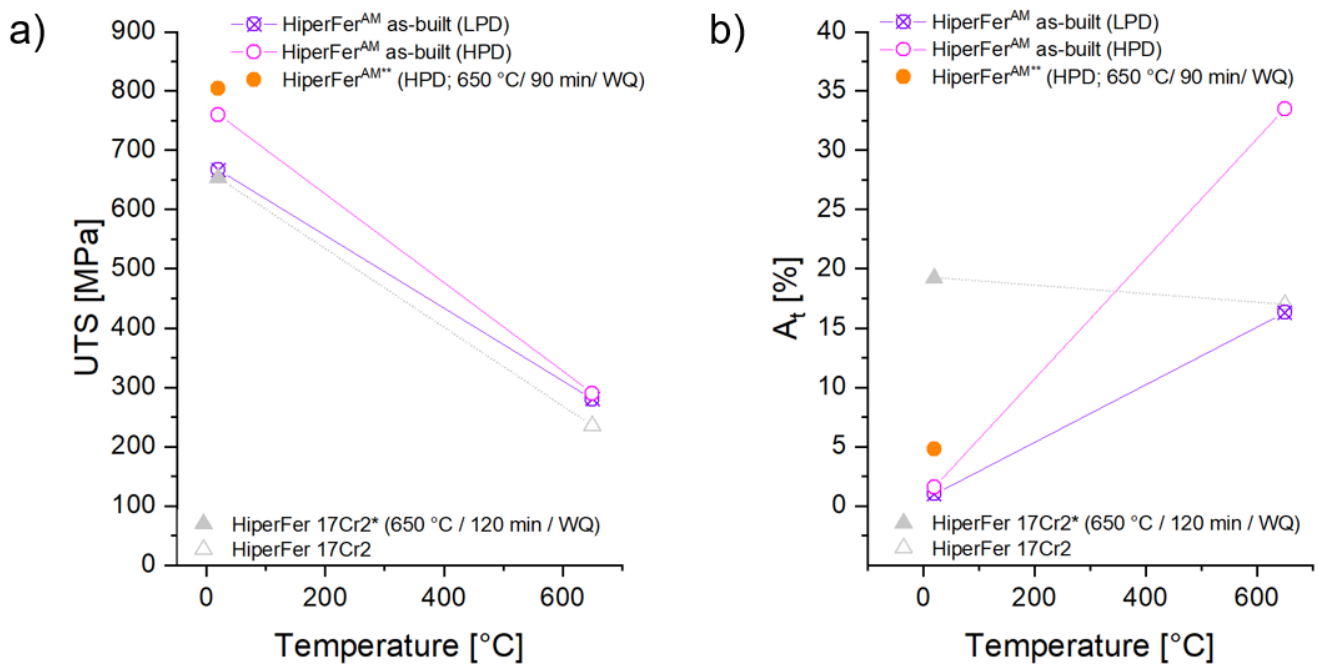
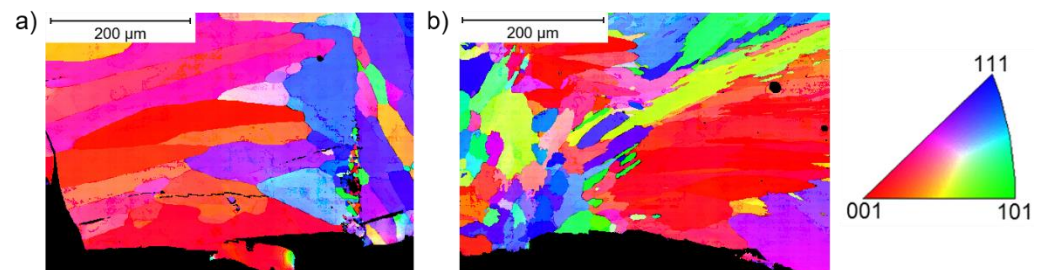


Figure 11. (a) UTS and (b) rupture elongation (A_t) of the 17Cr2 and HiperFer^{AM} variants (LPD and HPD) at 20 °C and 650 °C. HT: * 650 °C/120 min, ** 650 °C/90 min.

Table 3. UTS (20 and 650 °C) values and A_t of HiperFer 17Cr2 compared with the HiperFer^{AM} LPD and HPD variants.

Material	Heat-Treatment State	Area-Specific Laser Power (Wmm^{-2})	Test Temperature (°C)	UTS (MPa)	A_t (%)
HiperFer 17Cr2	650 °C/120 min	-	20	653	19.2
HiperFer 17Cr2	-	-	650	235	17
HiperFer ^{AM}	As-built	1050 (HPD)	20	760	1.6
HiperFer ^{AM}	As-built	195 (LPD)	20	667	1
HiperFer ^{AM}	650 °C/90 min	1050 (HPD)	20	804	4.8
HiperFer ^{AM}	As-built	1050 (HPD)	650	290	33.5
HiperFer ^{AM}	As-built	195 (LPD)	650	280	16.3

The advantage of HiperFer^{AM} (HPD) over HiperFer^{AM} (LPD) in terms of the UTS was caused by the smaller grain size (Figure 12) and the increased level of residual stress (i.e., higher area-specific power input). The ambient temperature rupture elongations of both the additively manufactured variants had expectedly low values of 1% (LPD) and 1.6% (HPD). In contrast, conventionally produced 17Cr2 yielded ~17% fracture elongation. In accordance with the encountered low fracture elongations at ambient temperature, the EBSD mappings of the additively manufactured tensile specimens present hardly any deformation (Figure 12), which was most likely caused by a comparatively high level of residual stress that resulted from the additive manufacturing process (hardness LPD/HPD 199/226 HV1, cf. Table 4).

**Figure 12.** HiperFer^{AM} (a) LPD and (b) HPD EBSD mappings taken perpendicularly to the fracture surfaces after the tensile experiments at ambient temperature.**Table 4.** Hardnesses of LPD and HPD HiperFer^{AM} in the as-built state and after compression creep testing.

Material	Hardness, As-Built State (HV1)				Hardness, After Creep Compression Test (HV1)			
	Mean	Min.	Max.	Range	Mean	Min.	Max.	Range
HiperFerAM LPD-L	199	193	209	16	211	197	222	25
HiperFerAM HPD-L	226	217	233	16	248	239	252	13
HiperFerAM LPD-Q	196	186	201	15	218	206	226	20
HiperFerAM HPD-Q	233	217	244	27	252	240	272	32

To evaluate whether high residual stress was the root cause for the low ambient temperature fracture strain, additively manufactured (HPD) tensile specimens were heat-treated at 650 °C for 90 min and subsequently tensile tested at ambient temperature. This heat treatment increased the fracture elongation by an approximate factor of 3 to a value of ~5%, while the UTS further increased to about 800 MPa (cf. Figure 11 and Table 3).

A conclusive assessment of the high level of residual stress as the reason for the low ambient temperature ductility was not possible because any heat treatment for stress reduction potentially led to the precipitation of additional strengthening Laves phase particles.

However, in view of the tensile properties at 650 °C, this assumption was reasonable. At 650 °C, HiperFer^{AM} (HPD) reached UTS/fracture elongation values of 290 MPa/33.5%, which constituted a remarkable improvement over conventionally produced HiperFer 17Cr2 sheet material (UTS: 235 MPa, A_t: 17%, cf. Figure 11 and Table 3). Concerning the UTS, no significant difference existed when applying the LPD parameters (cf. Figure 11 and Table 3), but the total fracture elongation diminished to about 16%, which still correlated well with the conventionally rolled sheet material. In the LPD HiperFer^{AM}, localized sub-grain formation was observed (Figure 13a), while global sub-graining occurred in the HPD variant (Figure 13c). Since the deformation conditions in the tensile test were identical, a higher stacking fault energy (i.e., the ability of dislocations for transversal slip) in the HPD variant caused by the adjusted AM parameters could have been responsible for the global subgrain formation.

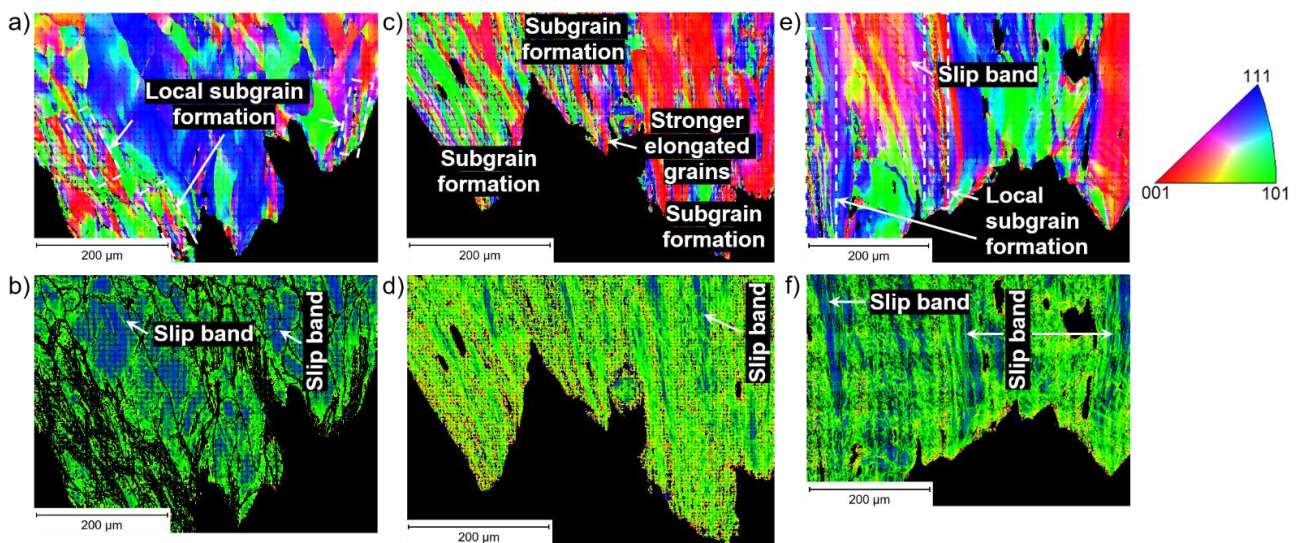


Figure 13. EBSD- and misorientation mappings taken longitudinally to the fracture surfaces after the tensile tests at 650 °C on HiperFer^{AM} manufactured with (a,b) LPD and (c,d) HPD, as well as on (e,f) conventional HiperFer 17Cr2.

Effective grain refinement caused by the high degree of global sub-grain formation obviously yielded higher plastic deformability (Figure 13d) in the case of the HPD variant. From a comparison of Figure 13a,b (LPD), limited dislocation activity and/or plastic deformation in sub-grain free areas was evident, which indicates that deformation preferentially occurred due to sub-grain formation. This explained the significantly increased ductility of the specimens that were manufactured when applying HPD. In conventionally produced HiperFer 17Cr2 sheet material, local sub-grain formation occurred similarly to the LPD HiperFer^{AM} (Figure 13a,e) variant, which explained the matching fracture elongations. Moreover, a stronger tendency toward slip band formation was observed in the conventionally produced HiperFer 17Cr2 (cf. Figure 13b,d–f).

Minimum creep rates of the HiperFer^{AM} variants were determined with respect to the build direction (longitudinal (L) and transversal (T)) at 650 °C (Figure 14). In the compression creep experiments, the LPD-manufactured HiperFer^{AM} specimens already exhibited unexpectedly high creep rates $> 10^{-4} \text{ h}^{-1}$ at a stress of 70 MPa, while much higher stress (130 MPa) was needed for the HPD specimens. The behavior that occurred in the LPD variant is referred to as “Power Law Breakdown (PLB)” [57]. At high stresses, higher strain rates occur more often than predicted by the power law relationship. This behavior is known as PLB. The cause for the PLB of LPD-manufactured HiperFer^{AM} at comparatively low stress was a pronounced change in the grain structure: In the as-built state, the microstructure consisted of directionally solidified (Figure 15a) grains, which then changed to a globularly recrystallized microstructure (Figure 15b) during the execution of the

compression creep experiment. A directionally solidified microstructure obviously cannot effectively be stabilized by Laves phase precipitation and should therefore be avoided. In contrast, the microstructure of the HPD variant remained stable. Only the grain width of the directional grains between the globular ones tended to decrease (cf. Figure 15c,d). The increased creep strength of the HPD manufactured HiperFer^{AM} was based on this stable microstructure. The building direction only had a minor impact on the minimum creep rates measured. Compared with HiperFer 17Cr2, the minimum creep rate in the first HPD-manufactured HiperFer^{AM} variant (mechanically alloyed) was only about 0.5 to 1 order of magnitude higher (with a tendency of decreasing discrepancy toward higher stress (Figure 14)). This indicates a good potential for high-temperature application of additively processed HiperFer steel. The white dots in Figure 15a,c were incompletely melted tungsten clusters (cf. Figure 7)

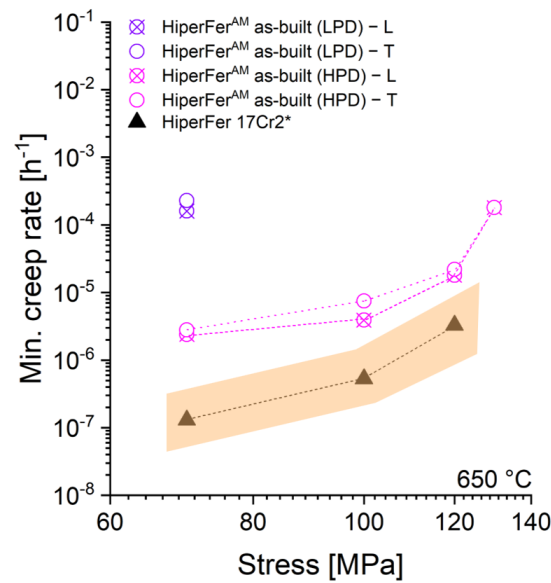


Figure 14. A 650 °C Norton plot of HiperFer^{AM} with respect to the area-specific laser power and build direction in comparison to HiperFer 17Cr2* Data from [13].

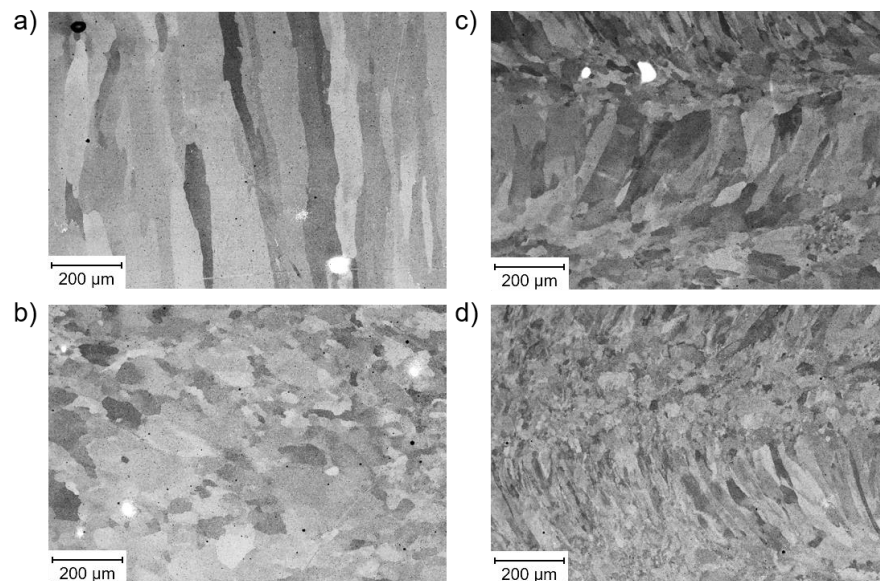


Figure 15. Comparison of as-built and post-compression creep experiment microstructures (specimens taken longitudinally to build direction). LPD: (a) as-built and (b) after compression creep. HPD: (c) as-built and (d) after compression creep.

Furthermore, the hardness increased after the compression creep testing, independently of the applied area-specific laser power and the building direction (Table 4). This indicates the high strengthening potential of HiperFer^{AM}.

4. Conclusions

The first high-chromium, Laves-phase-strengthened HiperFer^{AM} alloy that benefits from the additive manufacturing process and counteracting process-related defects, such as pores due to thermomechanically triggered [9,33] Laves phase precipitation, was developed.

Specific adjustment of the AM process parameters directly allowed for controlling the microstructural parameters, such as the grain size/morphology, as well as the size and number of the Laves phase particles, and thus, the resulting mechanical properties. At ambient temperature, UTS values of ~667/~760 MPa (LPD/HPD) were achieved in the as-built condition, with an elongation at fracture of ~1/1.6%. Subsequent stress relief due to the annealing of HiperFer^{AM} HPD resulted in a nearly tripled elongation at rupture and a UTS beyond 800 MPa. At 650 °C, the UTS of the HiperFer^{AM} HPD variant was 55 MPa higher in comparison to the HiperFer 17Cr2 sheet material, with almost doubled elongation at rupture (~33.5%). Global sub-grain formation during plastic deformation was argued to be the reason for the increased elongation at rupture. In general, additive manufacturing was found to produce smaller grain sizes than conventional manufacturing ($\leq 200/\sim 500$ μm).

Furthermore, the minimum creep rates of the HiperFer^{AM} HPD variant ranged from approximately 0.5 to 1 order of magnitude higher than that of conventionally produced HiperFer 17Cr2. In contrast, the LPD variant exhibited premature power-law breakdown under creep loading, which was caused by instability of the directionally solidified as-built grain structure. Creep properties did not show a dependency on build direction.

This first mechanically alloyed HiperFer^{AM} custom-made variant for the additive manufacturing process demonstrated high potential for high-temperature application. Furthermore, the substitution of comparatively expensive austenitic 316L steel in a small (special) series of ambient temperature components could be a realistic option. After grain size optimization and stress relief annealing, the resulting HiperFer^{AM} material may offer a UTS of about 1 GPa at a reasonably lower cost.

5. Outlook

The presented HiperFer^{AM} alloy will serve as a basis for further alloy development and optimization with a focus on tailored precipitation kinetics. To achieve this, thermokinetic simulations will be performed. In addition, the production of pre-alloyed powders for the LPBF process will be carried out. Further research will focus on the production of tailored microstructures with increased control over the in-built precipitation heat treatment and residual stress reduction by varying the AM process parameters and integrating substrate heating.

Author Contributions: Conceptualization, T.F. and B.K.; methodology, T.F., B.K. and X.F.; software, T.F., validation, T.F., B.K. and M.B.W., formal analysis, T.F., B.K., X.F. and M.B.W.; LMD manufacturing, M.B.W., investigation, T.F., B.K. and M.B.W., resources, B.K.; data curation, T.F., writing—original draft preparation, T.F.; writing—review and editing: B.K. and M.B.W.; visualization, T.F.; project administration, T.F. and B.K. All authors have read and agreed to the published version of the manuscript.

Funding: This research was funded by the German Helmholtz Society framework programme “Energy Efficiency, Materials and Resources”.

Institutional Review Board Statement: Not applicable.

Informed Consent Statement: Not applicable.

Data Availability Statement: Not applicable.

Acknowledgments: The authors would like to acknowledge the support of B. Werner and H. Reiners for the mechanical testing, V. Gutzeit and J. Bartsch for the sample preparation, and E. Wessel and D. Grüner for performing the microstructural investigations.

Conflicts of Interest: The authors declare no conflict of interest.

References

1. Khorasani, M.; Ghasemi, A.; Leary, M.; Sharabian, E.; Cordova, L.; Gibson, I.; Downing, D.; Bateman, S.; Brandt, M.; Rolfe, B. The effect of absorption ratio on melt pool features in laser-based powder bed fusion of IN718. *Opt. Laser Technol.* **2022**, *153*, 108263. [[CrossRef](#)]
2. Zhao, Y.; Koizumi, Y.; Aoyagi, K.; Yamanaka, K.; Chiba, A. Thermal properties of powder beds in energy absorption and heat transfer during additive manufacturing with electron beam. *Powder Technol.* **2021**, *381*, 44–54. [[CrossRef](#)]
3. Khan, H.M.; Waqar, S.; Koç, E. Evolution of temperature and residual stress behavior in selective laser melting of 316L stainless steel across a cooling channel. *Rapid Prototyp. J.* **2022**, *28*, 1272–1283. [[CrossRef](#)]
4. Singh, A.K.; Mundada, Y.; Bajaj, P.; Wilms, M.B.; Patil, J.; Kumar Mishra, S.; Jäggle, E.A.; Arora, A. Investigation of temperature distribution and solidification morphology in multilayered directed energy deposition of Al-0.5Sc-0.5Si alloy. *Int. J. Heat Mass Transf.* **2022**, *186*, 122492. [[CrossRef](#)]
5. Nespoli, A.; Bennato, N.; Villa, E.; Passaretti, F. Study of anisotropy through microscopy, internal friction and electrical resistivity measurements of Ti-6Al-4V samples fabricated by selective laser melting. *Rapid Prototyp. J.* **2022**, *28*, 1060–1075. [[CrossRef](#)]
6. Kürsteiner, P.; Bajaj, P.; Gupta, A.; Wilms, M.B.; Weisheit, A.; Li, X.; Leinenbach, C.; Gault, B.; Jäggle, E.A.; Raabe, D. Control of thermally stable core-shell nano-precipitates in additively manufactured Al-Sc-Zr alloys. *Addit. Manuf.* **2020**, *32*, 100910. [[CrossRef](#)]
7. Kürsteiner, P.; Wilms, M.B.; Weisheit, A.; Gault, B.; Jäggle, E.A.; Raabe, D. High-strength Damascus steel by additive manufacturing. *Nature* **2020**, *582*, 515–519. [[CrossRef](#)]
8. Kürsteiner, P.; Wilms, M.B.; Weisheit, A.; Barriobero-Vila, P.; Jäggle, E.A.; Raabe, D. Massive nanoprecipitation in an Fe-19Ni-xAl maraging steel triggered by the intrinsic heat treatment during laser metal deposition. *Acta Mater.* **2017**, *129*, 52–60. [[CrossRef](#)]
9. Fischer, T.; Kuhn, B.; Rieck, D.; Schulz, A.; Trieglaff, R.; Wilms, M.B. Fatigue Cracking of Additively Manufactured Materials—Process and Material Perspectives. *Appl. Sci.* **2020**, *10*, 5556. [[CrossRef](#)]
10. Barriobero-Vila, P.; Artzt, K.; Stark, A.; Schell, N.; Siggel, M.; Gussone, J.; Kleinert, J.; Kitsche, W.; Requena, G.; Haubrich, J. Mapping the geometry of Ti-6Al-4V: From martensite decomposition to localized spheroidization during selective laser melting. *Scr. Mater.* **2020**, *182*, 48–52. [[CrossRef](#)]
11. Rittinghaus, S.-K.; Amr, A.; Hecht, U. Intrinsic heat treatment of an additively manufactured medium entropy AlCrFe2Ni2-alloy. *Met. Mater. Int.* **2022**. [[CrossRef](#)]
12. Yakout, M.; Elbestawi, M.A.; Veldhuis, S.C.; Nangle-Smith, S. Influence of thermal properties on residual stresses in SLM of aerospace alloys. *Rapid Prototyp. J.* **2019**, *26*, 213–222. [[CrossRef](#)]
13. Mishrunova, T.; Artzt, K.; Haubrich, J.; Requena, G.; Bruno, G. Exploring the correlation between subsurface residual stresses and manufacturing parameters in laser powder bed fused Ti-6Al-4V. *Metals* **2019**, *9*, 261. [[CrossRef](#)]
14. Piscopo, G.; Salmi, A.; Atzeni, E. Influence of high-productivity process parameters on the surface quality and residual stress state of AISI 316L components produced by directed energy deposition. *J. Mater. Eng. Perform.* **2021**, *30*, 6691–6702. [[CrossRef](#)]
15. Giganto, S.; Martinnez-Pellitero, S.; Cuesta, E.; Zapico, P.; Barreiro, J. Proposal of design rules for improving the accuracy of selective laser melting (SLM) manufacturing using benchmarks parts. *Rapid Prototyp. J.* **2022**, *28*, 1129–1143. [[CrossRef](#)]
16. Kies, F.; Wilms, M.B.; Pirch, N.; Pradeep, K.G.; Schleifenbaum, J.H.; Haase, C. Defect formation and prevention in directed energy deposition of high-manganese steels and the effect on mechanical properties. *Mater. Sci. Eng. A* **2020**, *772*, 138688. [[CrossRef](#)]
17. Ikeda, T.; Yonehara, M.; Ikeshoji, T.-T.; Nobuki, T.; Hatate, M.; Kuwabara, K.; Otsubo, Y.; Kyogoku, H. Influences of process parameters on the microstructure and mechanical properties of CoCrFeNiTi based high-entropy alloy in a laser powder bed fusion process. *Crystals* **2021**, *11*, 549. [[CrossRef](#)]
18. Linares, J.-M.; Chaves-Jacob, J.; Lopez, Q.; Sprauel, J.-M. Fatigue life optimization for 17-4Ph steel produced by selective laser melting. *Rapid Prototyp. J.* **2022**, *28*, 1182–1192. [[CrossRef](#)]
19. Bajaj, P.; Hariharan, A.; Kini, A.; Kürsteiner, P.; Raabe, D.; Jäggle, E.A. Steels in additive manufacturing: A review of their microstructure and properties. *Mater. Sci. Eng. A* **2020**, *772*, 138633. [[CrossRef](#)]
20. Wolff, S.; Lee, T.; Faierson, E.; Ehmann, K.; Cao, J. Anisotropic properties of directed energy deposition (DED)-processed Ti-6Al-4V. *J. Manuf. Processes* **2016**, *24*, 397–405. [[CrossRef](#)]
21. Davies, C.M.; Thomlinson, H.; Hooper, P.A. Fatigue Crack Initiation and Growth Behaviour of 316L Stainless Steel Manufactured Through Selective Laser Melting. In Proceedings of the ASME 2017 Pressure Vessels and Piping Conference, Volume 6A: Materials and Fabrication, Waikoloa, HI, USA, 26 October 2017. [[CrossRef](#)]
22. Yadollahi, A.; Shamsaei, N.; Thompson, S.M.; Elwany, A.; Bian, L. Effects of building orientation and heat treatment on fatigue behavior of selective laser melted 17-4 PH stainless steel. *Int. J. Fatigue* **2017**, *94*, 218–235. [[CrossRef](#)]
23. Zhang, M.; Sun, C.-N.; Zhang, X.; Wei, J.; Hardacre, D.; Li, H. High cycle fatigue and ratcheting interaction of laser powder bed fusion stainless steel 316L: Fracture behaviour and stress-based modelling. *Int. J. Fatigue* **2019**, *121*, 252–264. [[CrossRef](#)]

24. Blinn, B.; Klein, M.; Gläßner, C.; Smaga, M.; Aurich, J.C.; Beck, T. An investigation of the microstructure and fatigue behavior of additively manufactured AISI 316L stainless steel with regard to the influence of heat treatment. *Metals* **2018**, *8*, 220. [[CrossRef](#)]
25. Kuhn, B.; Talik, M. HiperFer—High Performance Ferritic Steels. In *Proceedings of the 10th Liège Conference on Materials for Advanced Power Engineering*; Schriften des Forschungszentrums Jülich Reihe Energie & Umwelt/Energy & Environment: Liège, Belgium, 2014; Volume 234, pp. 264–273. ISBN 978-3-95806-000-5. (In Belgium)
26. Kuhn, B.; Talik, M.; Niewolak, L.; Zurek, J.; Hattendorf, H.; Ennis, P.J.; Quadackers, W.J.; Beck, T.; Singheiser, L. Development of High Chromium Ferritic Steels Strengthened by Intermetallic Phases. *Mater. Sci. Eng. A* **2014**, *594*, 372–380. [[CrossRef](#)]
27. Kuhn, B.; Lopez Barrilao, J.; Fischer, T. “Reactive” microstructure, the key to cost-effective, fatigue-resistant high temperature structural materials. In *Proceedings of the Joint EPRI-123HiMAT International Conference on Advances in High Temperature Materials*, Nagasaki, Japan, 21–24 October 2019; ISBN 13 987-1-62708-271-6.
28. Hsiao, Z.W.; Kuhn, B.; Yang, S.M.; Yang, L.C.; Huang, S.Y.; Singheiser, L.; Kuo, J.C.; Lin, D.Y. The Influence of Deformation on the Precipitation Behavior of a Ferritic Stainless Steel. In *Proceedings of the 10th Liège Conference on Materials for Advanced Power Engineering*, Schriften des Forschungszentrums Jülich/Energy & Environment, Liege, Belgium, 14–17 September 2014; Lecomte-Beckers, J., Dedry, O., Oackey, J., Kuhn, B., Eds.; Forschungszentrum Jülich GmbH Zentralbibliothek: Julich, Germany, 2014; Volume 94, pp. 349–358.
29. Pöpperlová, J.; Fan, X.; Kuhn, B.; Bleck, W.; Krupp, U. Impact of Tungsten on Thermomechanically Induced Precipitation of Laves Phase in High Performance Ferritic (HiperFer) Stainless Steels. *Appl. Sci.* **2020**, *10*, 4472. [[CrossRef](#)]
30. Fan, X.; Kuhn, B.; Pöpperlová, J.; Bleck, W.; Krupp, U. Thermomechanically Induced Precipitation in High Performance Ferritic (HiperFer) Stainless Steels. *Appl. Sci.* **2020**, *10*, 5713. [[CrossRef](#)]
31. Fan, X.; Kuhn, B.; Pöpperlová, J.; Bleck, W.; Krupp, U. Compositional Optimization of High-Performance Ferritic (HiperFer) Steels—Effect of Niobium and Tungsten Content. *Metals* **2020**, *10*, 1300. [[CrossRef](#)]
32. Kuhn, B.; Talik, M.; Fischer, T.; Fan, X.; Yamamoto, Y.; Lopez Barrilao, J. Science and technology of high performance ferritic (HiperFer) Stainless Steels. *Metals* **2020**, *10*, 463. [[CrossRef](#)]
33. Kuhn, B.; Barrilao, J.L.; Fischer, T. Impact of Thermomechanical Fatigue on Microstructure Evolution of a Ferritic-Martensitic 9 Cr and a Ferritic, Stainless 22 Cr Steel. *Appl. Sci.* **2020**, *10*, 6338. [[CrossRef](#)]
34. Blinn, B.; Görzen, D.; Fischer, T.; Kuhn, B.; Beck, T. Analysis of the Thermomechanical Fatigue Behavior of Fully Ferritic High Chromium Steel Crofer[®]22 H with Cyclic Indentation Testing. *Appl. Sci.* **2020**, *10*, 6461. [[CrossRef](#)]
35. Froitzheim, J.; Meier, G.H.; Niewolak, L.; Ennis, P.J.; Hattendorf, H.; Singheiser, L. Development of high strength ferritic steel for interconnect application in SOFCs. *J. Power Sources* **2008**, *178*, 163–173. [[CrossRef](#)]
36. National Board Inspection Code (NBIC). *Part-3 National Board Inspection Code*; ASME Press: New York, NY, USA, 2011.
37. ASME BPV Code. *Section III, Division 1: Rules for Construction of Nuclear Facility Components*; ASME Press: New York, NY, USA, 2019.
38. Welding Technology Institute of Australis. (WTIA) publication, TGN-PE-02, *Temper Bead Welding, Rev0,1*; Welding Technology Institute of Australia: Pymble, Australia, 2006.
39. ASME BPVC. *Section IX-Welding, Brazing, and Fusing Qualifications*; ASME Press: New York, NY, USA, 2015.
40. Talik, M.; Kuhn, B. High Temperature Mechanical Properties of a 17wt%Cr High Performance Ferritic (HiperFer) Steel Strengthened by Intermetallic Laves Phase Particles. In *Proceedings of the 9th International Charles Parsons Turbine and Generator Conference*, Loughborough, UK, 15–17 September 2015.
41. *DIN EN 10002-5:1992-02*; Zugversuch, Prüfverfahren bei erhöhter Temperatur, DIN Deutsches Institut für Normung e. V. Beuth Verlag GmbH: Berlin, Germany, 1991.
42. *DIN EN ISO 6892-2:2011-05*; Metallische Werkstoffe-Zugversuch-Teil 2: Prüfverfahren bei erhöhter Temperatur, DIN Deutsches Institut für Normung e. V. Beuth Verlag GmbH: Berlin, Germany, 2011.
43. *DIN EN ISO 6507-1:2018*; Metallic Materials-Vickers Hardness Test-Part 1: Test method (ISO 6507-1:2018). Beuth Verlag GmbH: Berlin, Germany, 2018.
44. Barrilao, J.L.; Kuhn, B.; Wessel, E. Identification, size classification and evolution of Laves phase precipitates in high chromium, fully ferritic steels. *Micron* **2017**, *101*, 221–231. [[CrossRef](#)] [[PubMed](#)]
45. Sim, G.M.; Ahn, J.C.; Hong, S.C.; Lee, K.J.; Lee, K.S. Effect of Nb precipitate coarsening on the high temperature strength in Nb containing ferritic stainless steels. *Mater. Sci. Eng. A* **2005**, *396*, 159–165. [[CrossRef](#)]
46. Hosoi, Y.; Wade, N.; Kunimitsu, S.; Urita, T. Precipitation behavior of Laves phase and its effect on toughness of 9Cr-2Mo Ferritic-martensitic steel. *J. Nucl. Mater.* **1986**, *141*, 461–467. [[CrossRef](#)]
47. Suo, J.; Peng, Z.; Yang, H.; Chai, G.; Yu, M. Formation of Laves Phase in Sanicro 25 Austenitic Steel during Creep-Rupture Test at 700 °C. *Metallogr. Microstruct. Anal.* **2019**, *2*, 281–286. [[CrossRef](#)]
48. Aghajani, A.; Richter, F.; Somsen, C.; Fries, S.G.; Steinbach, I.; Eggeler, G. On the formation and growth of Mo-rich Laves phase particles during long-term creep of a 12% chromium tempered martensite ferritic steel. *Scr. Mater.* **2009**, *61*, 1068–1071. [[CrossRef](#)]
49. Guo, J.T.; Zhou, L.Z. The Effect of Phosphorus, Sulphur and Silicon on Segregation, Solidification and Mechanical Properties of Cast Alloy 718. In *Proceedings of the 8th International Symposium on Superalloys*, Seven Springs Mountain Resort, Champion, PA, USA, 22–26 September 1996; pp. 451–458.
50. Kato, Y.; Ito, M.; Kato, Y.; Furukimi, O. Effect of Si on Precipitation Behavior of Nb-Laves Phase and Amount of Nb in Solid Solution at Elevated Temperature in High Purity 17%Cr-0.5%Nb Steels. *Mater. Trans.* **2010**, *51*, 1531–1535. [[CrossRef](#)]

51. Niewolak, L.; Savenko, A.; Grüner, D.; Hattendorf, H.; Breuer, U.; Quadackers, W.J. Temperature Dependence of Laves Phase Composition in Nb, W and Si-Alloyed High Chromium Ferritic Steels for SOFC Interconnect Applications. *JPEDAV* **2015**, *36*, 471–484. [[CrossRef](#)]
52. Vo, N.Q.; Liebscher, C.H.; Rawlings, M.J.S.; Asta, M.; Dunand, D.C. Creep properties and microstructure of a precipitation-strengthened ferritic Fe–Al–Ni–Cr alloy. *Acta Mater.* **2014**, *71*, 89–99. [[CrossRef](#)]
53. Fan, X. Optimization of Laves Phase Strengthened High Performance Ferritic Stainless Steels. Ph.D. Thesis, RWTH Aachen, Aachen, Germany, 2020. Available online: <https://publications.rwth-aachen.de/record/792517/files/792517.pdf> (accessed on 19 May 2022). [[CrossRef](#)]
54. Kuhn, B.; Fischer, T.; Fan, X.; Talik, M.; Aarab, F.; Yamamoto, Y. HiperFer-Weiterentwicklungs-Und Anwendungspotenziale. In Proceedings of the 43th FVWHT Vortragsveranstaltung Langzeitverhalten Warmfester Stähle und Hochtemperaturwerkstoffe, Online, 27 November 2020; p. 43.
55. Kuhn, B.; Talik, M.; Lopez Barrilao, J.; Singheiser, L. Microstructure stability of ferritic-martensitic, austenitic and fully ferritic steels under fluctuating loading conditions. In Proceedings of the 1st 123rd HiMat Conference, Sapporo, Japan, 29 June–3 July 2015.
56. Zhang, Q.; Zhu, Y.; Gao, X.; Wu, Y.; Hutchinson, C. Training high-strength aluminum alloys to withstand fatigue. *Nat Commun.* **2020**, *11*, 5198. [[CrossRef](#)]
57. Lesuer, D.R.; Syn, C.K.; Sherby, O.D. *An Evaluation of Power Law Breakdown in Metals, Alloys, Dispersion Hardened Materials and Compounds*; Lawrence Livermore National Lab.(LLNL): Livermore, CA, USA, 1999.